PCCP

CASPT2 molecular geometries of Fe(II) spin-crossover complexes

Journal:	*Physical Chemistry Chemical Physics*
Manuscript ID	CP-ART-10-2021-004885.R1
Article Type:	Paper
Date Submitted by the Author:	14-Dec-2021
Complete List of Authors:	Finney, Brian; University of South Dakota, Department of Chemistry Roy Chowdhury, Sabyasachi; University of South Dakota, Department of Chemistry Kirkvold, Clara; University of South Dakota, Department of Chemistry Vlaisavljevich, Bess; University of South Dakota, Department of Chemistry

Journal Name

ARTICLE TYPE

Cite this: DOI: 00.0000/xxxxxxxxxx

CASPT2 molecular geometries of Fe(II) spin-crossover complexes†

Brian A. Finney, Sabyasachi Roy Chowdhury, Clara Kirkvold, and Bess Vlaisavljevich*

Received Date
Accepted Date

DOI: 00.0000/xxxxxxxxxx

Using fully internally contracted (FIC)-CASPT2 analytical gradients, geometry optimizations of spin-crossover complexes are reported. This approach is tested on a series of Fe(II) complexes with different sizes, ranging from 13 to 61 atoms. A combination of active space and basis set choices are employed to investigate their role in determining reliable molecular geometries. The reported strategy demonstrates that a wave function-based level of theory can be used to optimize the geometries of metal complexes in reasonable times and enables one to treat the molecular geometry and electronic structure of the complexes using the same level of theory. For a series of smaller Fe(II) SCO complexes, strong field ligands in the LS state result in geometries with the largest differences between DFT and CASPT2; however, good agreement overall is observed between DFT and CASPT2. For the larger complexes, moderate sized basis sets yield geometries that compare well with DFT and available experimental data. We recommend using the (10e,12o) active space since convergence to a minimum structure was more efficient than with truncated active spaces despite having similar Fe–ligand bond distances.

1 Introduction

Spin-crossover (SCO) is a phenomenon that occurs in a series of transition metal complexes where a transition between spin states takes place by means of external stimuli such as temperature, pressure, or light irradiation.[1,2] This can occur spontaneously in $d^4 - d^7$ transition metal complexes provided that the energy splitting between the high spin (HS) and low spin (LS) state is sufficiently small.[3] This property was first described by Cambi and Szegö in the early 1930s when they observed "magnetically isomeric forms" while studying the temperature dependence of the magnetic moments of an Fe(III) complex.[4,5] Later, Koenig and Madeja described the process as an equilibrium between the LS and HS states.[6] Although there are a substantial number of complexes showing SCO behavior, Fe(II) and Fe(III) complexes are most common. Owing to this inherent bistability, molecules exhibiting SCO have potential applications as building units in single molecule switches, optical displays, or data storage devices.[7,8]

Although ligand-field theory provides a qualitative description of the electronic structure of SCO complexes,[9] a comprehensive strategy with high-level electronic structure methods is necessary to obtain reasonably accurate chemical predictions of SCO behavior, specifically when evaluating spin-state energetics. Numerous density functional theory (DFT)[10] and wave function theory (WFT)[11–13]-based studies have predicted the electronic structure of such molecules accurately. DFT, with its wide range of exchange-correlation functionals, provides a useful way to evaluate molecular geometries, vibrational frequencies, entropy differences between HS and LS states, and other spectroscopic parameters of spin-crossover systems while offering computational efficiency.[14] However, it has been observed that many density functionals provide a good description of molecular geometries despite the fact that significant deviations in spin-state splitting energies are reported based on functional choice.[10,15,16] This is due to the biased nature of density functionals.[17] For example, pure density functionals using the standard generalized gradient approximation (GGA) stabilize the LS state as the ground spin state leading to large spin-state splitting energies, whereas hybrid functionals are reported to favor HS states.[10,14,17] The reparametrized version of B3LYP (so-called B3LYP*), which has 15% Hartree–Fock (HF) exchange compared to 20% in the original functional, has shown improved performance for transition metal complexes.[18,19] Although other functionals (with 10-15% HF exchange) tend to yield acceptable estimates of spin-state energies, none uniformly perform well for all molecular systems reported to date.[3,20]

Although WFN-based methods are significantly more computationally intensive than DFT, they can provide an accurate and systematically improvable description of spin state energetics. Among these methods, coupled cluster (CC) theory including single, double, and perturbative triple excitations (CCSD(T))

Address: 414 E Clark St., Vermillion, SD, 57069, USA E-mail: bess.vlaisavljevich@usd.edu

† Electronic Supplementary Information (ESI) available: [details of any supplementary information available should be included here]. See DOI: 00.0000/00000000.

is considered to be the "gold standard" in terms of including electron correlation in metal complexes;[21] however, its application is limited to molecular systems of moderate size and single-reference electronic structures. Note that domain-based local pair-natural orbital coupled cluster (DNLPO-CCSD(T)) combines near-CCSD(T) accuracy with DFT speed, allowing one to study much larger systems than was previously possible.[22–25] In complexes with multiconfigurational character, the complete active space self-consistent field (CASSCF)[26,27] method with corrections to the energy from second-order perturbation theory (CASPT2)[28–30] is frequently employed. CASPT2 requires a careful choice of orbitals in the so-called active space together with the appropriate basis set. This approach has been applied successfully to transition metal complexes and comparisons with DFT are available in literature.[12,13,31] Nevertheless, CASPT2 is known to bias the high-spin state,[21,32] due to the poor treatment of electron correlation arising from the semi-core $3s$ and $3p$ orbitals. To counter this effect, a combined CASPT2/CC approach is taken in which the valence electron correlation is treated with the multiconfigurational CASPT2 method with a large basis set and CCSD(T) with a limited basis is employed to treat the semi-core $3s3p$ correlation.[21]

Despite offering significant improvements in accurately determining the electronic structure, WFT-based methods are not routinely used in the geometry optimization of metal complexes, even now that analytical gradients are available.[33] This is due to the cost associated with molecular size as well as the fact that DFT generally yields reasonable geometries. Therefore, traditional approaches to investigate the electronic structures of the transition metal complexes and explore the spin-crossover mechanism employ a combined DFT and WFT approach. Geometry optimizations are carried out with DFT followed by subsequent treatment with CASPT2.

Nevertheless, in some Fe SCO complexes improved molecular geometries have been obtained by a "point-by-point" CASPT2 calculations varying the metal-ligand bond distances.[12,13,34] Each point consists of a structure where the metal-ligand distances are fixed and the remainder of the molecule is relaxed to the DFT equilibrium geometry. A benefit of this approach is that the effect of changing a particular geometric parameter on the electronic structure of the ground and excited states can be readily compared. However, this approach is only easily applicable if the molecule is symmetric where the metal-ligand bond distances can be stretched isotropically. This approach also cannot be used to compute vibrational frequencies at the higher level of theory since the resulting geometry is not a minimum on that surface.

Geometry optimizations of multiconfigurational species have been performed with CASSCF, but the absence of dynamic correlation results in an overestimation of the metal-ligand bond distances.[35] Until recently, CASPT2 geometry optimizations were limited to small molecules,[36] but bond distances improve with respect to CASSCF. In 2015, MacLeod *et al.* first implemented analytical nuclear gradients for fully internally contracted (FIC) state-specific (SS-)CASPT2 in the BAGEL program package.[33,37] This was later extended to include multi-state (MS-) and extended multi-state (XMS-)CASPT2.[37,38] The FIC gradients allow for the evaluation of nuclear gradients in larger molecules compared to the previously reported uncontracted[39–42] and partially internally contracted multireference methods (PIC)[43–45] which were applicable only to small systems since they treat a limited number of basis functions. To date, the molecular geometry of a handful of transition metal complexes have been computed with FIC-CASPT2 including the copper corrole,[38] an iron porphyrin,[46] and three Cr_2 complexes.[47]

In this article, we make use of FIC-CASPT2 analytical gradients to optimize a series of smaller octahedral Fe(II) SCO complexes with ligands ranging from weak to strong field (Figure 1). Then, we apply this approach to study four larger Fe(II) SCO complexes ranging in size from 49 to 61 atoms (Figure 2). The specific smaller Fe(II) SCO systems were chosen since they have been used by us and others to compare the performance of computational methods for spin-state energetics in SCO complexes.[12,13,48–51] On the other hand, the three larger complexes were chosen not only to be comparable with literature data, but also to represent different sized molecules. The medium-sized $[Fe(tacn)_2]^{2+}$ complex has 49 atoms and has been well-characterized by DFT and diffraction experiments.[52–54] While the $[Fe(pic)_3]^{2+}$ complex has the same number of atoms, but the symmetry around the Fe center is slightly reduced since there are two different types of N donors. Experimental structural data is available at different temperatures for both the LS and HS states.[55,56] Finally, the $[Fe(bpy)_2]^{2+}$ complex was chosen since it has been well-characterized experimentally,[57,58] previously studied with DFT and CASPT2,[11,12,59] and has 61 atoms demonstrating that FIC-CASPT2 optimizations can be performed for such systems. The Fe-N bond distances in $[Fe(bpy)_2]^{2+}$ were optimized point wise with CASPT2 as well.[11,12] We report the effects of basis set and active space on the resulting geometries. Computational time required for select systems is also included.

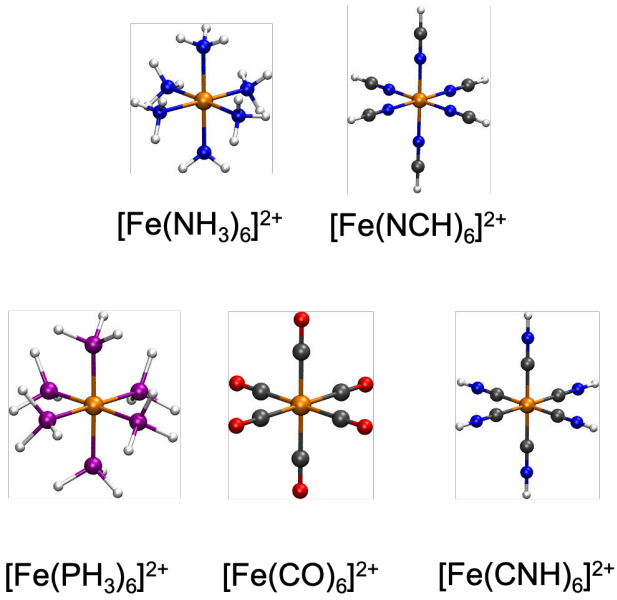

Fig. 1 Smaller octahedral Fe(II) SCO structures $[FeL_6]^{2+}$ where L = NH_3, NCH, CO, PH_3, and CNH.

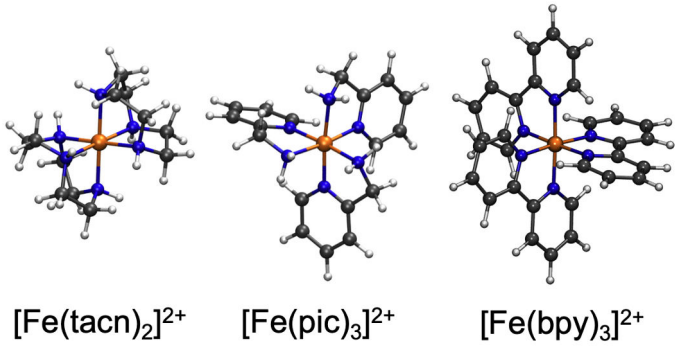

Fig. 2 Larger Fe(II) SCO structures studied in this work (tacn = 1,4,7-triazacyclononane, pic = picolylamine, and bpy = bipyridine).

2 Computational Details

Geometry optimizations are performed with (XMS)-CASPT2 as implemented in the BAGEL program package.[37,60] The XMS-CASPT2 approach is always used for the HS state and SS-CASPT2 is used for the LS state; however, we refer to the results as CASPT2 for simplicity. The HS quintet state is state averaged over three states while the lowest CI root is computed for the LS singlet state. The cc-pVTZ basis set[61] was used on all atoms for the so-called $[FeL_6]^{2+}$ species. The larger molecules in Section 3.3 were computed with the cc-pVTZ basis[61] on Fe and the cc-pVDZ basis[62] on the remaining atoms. Density fitting is used in all calculations with the def2-TZVPP-JKFIT auxiliary basis[63]. A vertical shift of 0.2 to 0.4 a.u. was used,[38] and the zero-order Hamiltonian does not employ the so-called IPEA shift. All CASSCF and CASPT2 energies were converged to 1.0×10^{-8} a.u. In the geometry optimization, the structure was considered converged when maximum component of the gradient was 3.0×10^{-4} a.u./Bohr, the maximum displacement was 1.12×10^{-3} Bohr, and the maximum change in energy was 1.0×10^{-6} a.u. Vibrational frequencies were computed for the LS and HS states of one system, $[Fe(tacn)_2]^{2+}$ with the cc-pVDZ basis set on all atoms and the ($6e$,$5o$) active space, confirming both as minima; however, vibrational analysis was not performed for the remaining systems.

The minimal active space would include the the Fe $3d$ orbitals and the corresponding six electrons, denoted ($6e$,$5o$). While we test the performance of this active space for geometry optimizations, it is well established that first row transition metals with a more than half filled d-shell require the inclusion of the so-called correlating $4d$ orbitals in the active space to improve the CASPT2 energy ($6e$,$10o$).[64] Finally, adding two doubly-occupied e_g ligand orbitals has been shown to yield a balanced description of important non-dynamical electron correlation effects in octahedral complexes, resulting in a ($10e$,$12o$) active space (Figure 3).[12,29,65] Geometry optimizations are performed with all three active spaces for the $[FeL_6]^{2+}$ complexes (Tables S1-S2) and $[Fe(tacn)_2]^{2+}$, while the other complexes are optimized with only the ($10e$,$12o$) active space.

For comparison, geometry optimizations were performed with DFT for all complexes using the PBE,[66] TPSSh,[67,68] M06,[69] and M06-L[70] functionals along with the def2-TZVP basis set[71] on all atoms as implemented in the Turbomole software package.[72] The resolution of the identity approximation was used.[73]

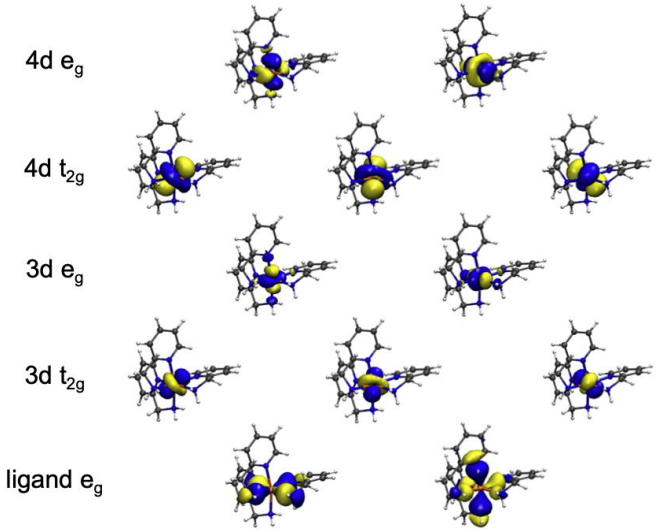

Fig. 3 CASSCF active natural orbitals for the $[Fe(pic)_3]^{2+}$ complex. An isovalue of 0.04 a.u. is used.

The relative energies between the HS and LS states, ΔE_{HL}, is evaluated on the $[FeL_6]^{2+}$ geometries using the CASPT2/CC approach (*vida supra*). Two sets of single point calculations with CCSD(T) were performed using the Orca program[74,75]: one in which the $3s$ and $3p$ electrons are correlated and one where they are not. The aug-cc-pwCVTZ basis set was used on Fe and cc-pVDZ was used on all other atoms.[61] From these calculations, the energy correction, ΔE_{3s3p}, is computed and added as to CASPT2 ΔE_{HL} to yield an improved prediction of CASPT2/CC ΔE_{HL}. CASPT2 single point calculations with a larger basis (denoted in the text for the specific complexes) are used to calculate CASPT2 ΔE_{HL} for the complexes in Figure 2.

3 Results and Discussion

The results are divided into four sections focused on the geometries of smaller Fe(II) complexes, spin-state splitting energies of smaller Fe(II) complexes, geometries of larger Fe(II) complexes, and a brief discussion of computational cost.

3.1 Geometries of Smaller Fe(II) Complexes

To investigate the performance of full CASPT2 geometry optimizations using analytical gradients, we performed geometry optimization of a series of smaller octahedral Fe(II) complexes with the general formula $[FeL_6]^{2+}$ where L includes ligands with varying ligand field strength (NH_3, NCH, CO, PH_3, and CNH) (Figure 1). Although some experimental data is available (Table 1),[76,77] the measurements were taken at finite temperatures and typically only one spin state was characterized. Therefore, we choose to directly compare CASPT2 and DFT optimized geometries since the comparison with experiment is less direct. We again emphasize that DFT geometries are in good agreement with available experimental data for these complexes.[76,77] Tests with smaller active spaces and basis sets are included in Table S2.

The CASPT2 computed Fe–L bond lengths are consistent with

Table 1 Average CASPT2/cc-pVTZ Fe–L bond distances (in Å) for $[FeL_6]^{2+}$ where L = NH_3, NCH, PH_3, CO and CNH. DFT/def2-TZVP distances are included for comparison. Diffraction data is included when available, where the temperature of the measurement is included in parentheses. Averages of the four DFT functionals are included as well.

L	Method	Fe–L bond length (Å)		
		HS_{apical}	$HS_{equatorial}$	LS
NH_3	CASPT2	2.263	2.258	2.058
	DFT Avg.	2.271	2.275	2.082
	TPSSh	2.294	2.276	2.080
	PBE	2.300	2.282	2.074
	M06-L	2.241	2.268	2.084
	M06	2.252	2.277	2.089
NCH	CASPT2	2.154	2.164	1.907
	DFT Avg.	2.175	2.166	1.935
	TPSSh	2.170	2.160	1.928
	PBE	2.176	2.150	1.908
	M06-L	2.192	2.190	1.960
	M06	2.162	2.167	1.943
	Crystal	2.159[77]	–	
PH_3	CASPT2	2.596	2.618	2.209
	DFT Avg.	2.602	2.635	2.259
	TPSSh	2.663	2.628	2.263
	PBE	2.582	2.629	2.248
	M06-L	2.574	2.603	2.250
	M06	2.622	2.643	2.274
CO	CASPT2	2.324	2.285	1.864
	DFT Avg.	2.338	2.268	1.922
	TPSSh	2.331	2.264	1.919
	PBE	2.319	2.220	1.894
	M06-L	2.358	2.301	1.940
	M06	2.345	2.288	1.933
	Crystal			1.910[76] (300K)
CNH	CASPT2	2.255	2.203	1.846
	DFT Avg.	2.251	2.209	1.900
	TPSSh	2.268	2.213	1.901
	PBE	2.260	2.179	1.882
	M06-L	2.175	2.201	1.886
	M06	2.302	2.244	1.918

those obtained from DFT optimizations (Table 1). We also report the average value of the four DFT functionals since one of the arguments one could make for using CASPT2 is that it does not depend on functional choice. We note that one can argue that CASPT2 introduces a dependence on the choice of active space; however, we argue that a geometry optimized with too small an active space is unlikely to yield physically meaningful bond distances and angles. A larger active space can then be employed in a systematically improvable fashion both for subsequent geometry optimization or to perform single-point calculations. Comparing the DFT average bond distances with CASPT2 for the HS state, the differences range from −0.017 to +0.021 Å (a positive value occurs when the CASPT2 bond distance is longer than the DFT average value). and no clear trend as a function of ligand field strength emerges with regard to geometry differences between the methods. On the other hand, the deviations between CASPT2 and DFT are larger for the LS bond distances, in particular for the strong field ligands PH_3, CO, and CNH where the difference between the CASPT2 and average DFT distance is −0.050, −0.057, and −0.051 Å, respectively. This can be compared with the weak field ligands NH_3 and NCH where the differences were 0.024 and −0.028 Å, respectively. Note that the complexes with strong field ligands tend to be more multiconfigurational (Tables S7 and S8).

Additionally, we compared the M-L bond lengths of the fully optimized $[Fe(NH_3)_6]^{2+}$ geometries with previously reported M-L bond lengths obtained by point-by-point CASPT2 calculations. The point-by-point computed Fe–N bond lengths were found to range from 2.243 to 2.256 Å for the HS state and 2.049 to 2.070 Å for the LS geometry, depending on the size of the basis set and the active space.[12] The CASPT2/cc-pVTZ optimized molecular geometries are in line with these results. The FIC-CASPT2 optimized geometries are slightly longer with average Fe-N distances for the HS apical bond distance at 2.263 Å, the HS equatorial bond distance at 2.258 Å, and the LS bond distance at 2.058 Å). These are small differences given that the basis set and zero-order Hamiltonian are not the same in the two sets of calculations.

Without a clear experimental reference, it is not possible to definitively assess if CASPT2 or DFT perform "better". Both have their strengths since DFT is less computationally intensive and converges more rapidly with respect to basis set choice, while CASPT2 can be used to systematically improve the treatment of electron correlation. These results support that CASPT2 geometries using reasonable sized basis sets and a modest sized active space choices result in reliable bond distances in Fe(II) SCO complexes. We also note greater differences in general, as determined by changes in the weight of the CI coefficients in CASSCF and the T1 amplitudes from coupled cluster (Tables S7 and S8), for the LS states compared to the HS states where more multiconfigurational character tends to be observed.

3.2 Spin State Splitting Energies of the Smaller Fe(II) Complexes

In order to understand the impact of the geometry changes discussed previously, CASPT2/CC ΔE_{HL} is computed on the molecular geometries optimized with CASPT2 and DFT (Table 2). Note that other methods can be used to compute ΔE_{HL}. Recently, Flöser *et al.* used detailed pair natural orbital-based (DLPNO) coupled cluster calculations for $[Fe(NH_3)_6]^{2+}$ and $[Fe(NCH)_6]^{2+}$ obtaining values of –11.3 and –8.8 kcal/mol, respectively, using a QZ/5Z quality basis set.[48] Additionally, we have previously reported CASPT2/CC values for the same complexes on the TPSSh geometry extrapolated to the basis set limit resulting in values of –14.8 and –3.7 kcal/mol.[50] As such, we emphasize once more the challenges associated with predicting SCO phenomenon quantitatively and that the values in Table 2 are presented to demonstrate sensitivity to choice of geometry, not the absolute best computation of ΔE_{HL}. First, strong field ligands stabilize complexes in the LS ground state, leading to more positive values of ΔE_{HL} in CO, PH_3, and CNH compared to the weak field NH_3 and NCH ligands. The standard deviation of ΔE_{HL} among the four DFT functionals is always less than 2 kcal/mol but appears to be larger for the strong field ligands. On the other hand, ΔE_{HL} computed using the CASPT2 geometries differs from the average value on the

DFT geometries from −5.5 to +0.3 kcal/mol. The CASPT2 and average DFT ΔE_{HL} are within 1.5 kcal/mol with the exception of $[Fe(NH_3)_6]^{2+}$ at -5.5 kcal/mol.

Table 2 CASPT2/CC computed ΔE_{HL} values in kcal/mol for $[FeL_6]^{2+}$ complexes using the CASPT2 and DFT optimized geometries. The difference from the CASPT2 value is reported in parentheses.

Method	NH_3	NCH	CO	PH_3	CNH
CASPT2	–36.2	–17.2	38.9	46.2	55.8
TPSSh	–41.5	–16.7	37.6	44.7	54.7
	(–5.4)	(+0.5)	(–1.2)	(–1.5)	(–1.1)
PBE	–41.0	–16.9	39.4	45.2	56.3
	(–4.9)	(+0.2)	(+0.6)	(–1.0)	(+0.5)
M06-L	–41.7	–16.8	36.5	45.8	56.9
	(–5.6)	(+0.3)	(–2.4)	(–0.4)	(+1.1)
M06	–42.5	–16.8	36.4	44.2	53.4
	(–6.3)	(+0.3)	(–2.5)	(–1.9)	(–2.3)
DFT avg.	–41.7	–16.8	37.5	45.0	55.3
DFT st. dev.	0.6	0.1	1.4	0.7	1.6

3.3 Geometries of Larger Fe(II) Complexes

In this section, the effect of active space and basis set choice for $[Fe(tacn)_2]^{2+}$ is discussed, followed by sections on the geometries of $[Fe(bpy)_3]^{2+}$ and asymmetric $[Fe(pic)_3]^{2+}$.

3.3.1 Effect of Active Space and Basis Set Choice for the $[Fe(tacn)_2]^{2+}$ Complex

The CASPT2 Fe–L bond distances in the studied $[FeL_6]^{2+}$ complexes are in good agreement with available experimental data and the average values from the DFT geometries. However, the $[FeL_6]^{2+}$ geometries were optimized with the largest basis set (cc-pVTZ) and active space (10*e*,12*o*) directly. For moderately sized molecular complexes (40-50 atoms), this becomes computationally intensive, while for the largest complexes the calculation is intractable. As such, we aim to use the smallest basis set and active space required to obtain reliable geometries, thereby using the fewest resources. We tested the effect of basis set and active space on the larger and less symmetric $[Fe(tacn)_2]^{2+}$ complex where tacn = 1,4,7-triazacyclononane (Figure 2). The complex was characterized by diffraction in 1985,[54] and its ability to undergo thermal spin-crossover at 330K was reported in 2013.[78]

CASPT2 geometry optimizations of $[Fe(tacn)_2]^{2+}$ were carried out with the active spaces (6*e*,5*o*), (6*e*,10*o*) and (10*e*,12*o*) along with four basis sets sizes: cc-pVDZ on all atoms, cc-pVTZ on Fe and cc-pVDZ on the other atoms, cc-pVTZ on Fe and its first coordination sphere and cc-pVDZ on the other atoms, and cc-pVTZ on all atoms (Table 3 and Table S3). Geometry optimizations that use the cc-pVDZ basis set on all atoms have longer Fe–N bond distances than those with triple-ζ on Fe. For example, Fe–N bond distances optimized using the (6*e*,5*o*) active space with the double-ζ basis were 2.044 Å in the LS state, but are 2.036 Å when Fe is treated with cc-pVTZ. Using cc-pVTZ on all atoms only changes these distances by 0.002 Å with respect to the distance with cc-pVTZ only on Fe. On the other hand, the $Fe-N_{equatorial}$ bond distance is nearly the same for all basis sets tested while the Fe–N_{apical} distance shows slightly more sensitivity to basis set choice. The choice of active space resulted in reasonably small changes in Fe–N bond distances in both the HS and LS state. The largest change from the (6*e*,5*o*) to the (10*e*,12*o*) is only 0.004 Å. Since the (10*e*,12*o*) active space has been reported to produce good agreement with the spin state energies and spin-crossover properties[34,79] of transition metal complexes, we decided to carry out rest of the geometry optimizations with this active space. We also tend to observe convergence in fewer geometry steps when this active space is used making the computational cost less in total despite being higher per gradient calculation. The cc-pVTZ basis set will be used on Fe only for the remaining calculations as well.

Considering this level of theory, the average CASPT2 optimized LS Fe–N bond lengths (2.036 Å) (Table 3) are in very good agreement with those of the crystal structure[54], where the Fe–N bond lengths vary between 2.023-2.042 Å (2.033 Å on average). We can also compare to the Fe–N distances with the reported geometries by different DFT methods.[52,53] Kepp obtained a distance of 2.031 Å at the BP86/def2-SVP/COSMO level of theory in the LS state, and for the HS state the average $Fe-N_{apical}$ and $Fe-N_{equatorial}$ distances were 2.242 and 2.238 Å, respectively.[52] These are 0.030 and 0.012 Å longer than the corresponding CASPT2 (10*e*,12*o*) values.

On the other hand, the DFT geometries computed by Lord *et al.* show the average LS Fe–N distance of 2.084 Å,[53] when they used reparametrized B3LYP* functional with the 6-31G** basis set for lighter elements and the LACVP basis for the Fe (0.049 Å longer than CASPT2). For the HS state, the average $Fe-N_{apical}$ and $Fe-N_{equatorial}$ bond distances were reported to be 2.273 Å and 2.266 Å, respectively (0.061 and 0.040 Å from CASPT2).[53] The difference between the two DFT calculations[52,53] were similar magnitudes of 0.031 and 0.028 Å for the HS apical and equatorial distances, with a difference of 0.053 Å in the LS state. DFT optimizations were performed with the same functionals as in Table 1 and are given in Table S4. Overall, the CASPT2 geometries of $[Fe(tacn)_2]^{2+}$ are in good agreement with both experimental and DFT data, falling within the differences typically observed due to functional dependence.

Table 3 Selected average Fe–N bond distances (in Å) as a function of basis set size and active space. The atoms with the cc-pVTZ basis set are noted; all remaining atoms are treated with cc-pVDZ. Apical and equatorial bond distances are given for the HS state.

Active Space	Atoms with cc-pVTZ	Fe–N Bond Length		
		HS_{apical}	$HS_{equatorial}$	LS
(6*e*,5*o*)	all	2.209	2.223	2.034
	Fe, N	2.207	2.222	2.035
	Fe	2.215	2.223	2.036
	none	2.216	2.223	2.044
(6*e*,10*o*)	Fe	2.213	2.226	2.037
(10*e*,12*o*)	Fe	2.212	2.226	2.035

3.3.2 Geometries of $[Fe(bpy)_3]^{2+}$

The $[Fe(bpy)_3]^{2+}$ complex, where bpy = 2,2′-bypyridine, is known to be stable in the LS spin state (Figure 2). Due to the large spin splitting energy ($\Delta E_{HL} \approx 6000$ cm^{-1}),[11] the molecule does not undergo thermal spin-crossover; however, irradiation with light

Table 4 Selected average CASPT2 Fe–L bond distances (in Å) of the complexes $[Fe(bpy)_3]^{2+}$, and $[Fe(pic)_3]^{2+}$.

Molecule	Fe–N Bond Lengths		
	Bond	HS	LS
$[Fe(bpy)_3]^{2+}$	$Fe-N_{apical}$	2.182	1.941
	$Fe-N_{equatorial}$	2.168	
$[Fe(pic)_3]^{2+}$	$Fe-N_{pyridine}$	2.187	1.964
	$Fe-N_{amine}$	2.234	2.029

results in excited state mediated population transfer from the LS to HS state.[80,81] Nevertheless, we are focusing on the geometries associated with the HS and LS states. For the LS geometry, we compare our results with experimental[57,58] and computational data.[11,12,59] Since experimental geometries are only available in the LS state,[57,58] the CASPT2 HS Fe–N bond lengths are compared to other computational results. The CASPT2 computed LS geometry has an average Fe–N bond length of 1.941 Å,[12] in nice agreement with reported experimental distances of 1.967 Å (a difference of 0.026 Å).[57,58] Depending on the choice of functional and basis set, literature values for the DFT computed Fe–N bond distances in the LS state vary from 1.956 to 2.027 Å.[59] Similarly, the DFT LS bond distances computed using the TPSSh, PBE, M06, and M06-L functionals and def2-TZVP basis sets varied from 1.968 to 2.009 Å (Table S5). In the HS geometry, the CASPT2 Fe–N bond lengths are on average 2.168 Å in the equatorial plane and 2.182 Å for the apical bonds, consistent with those reported by DFT that fall in the range of 2.148 to 2.234 Å.[59] Again, the DFT distances computed is this work compare well to the literature ranging from 2.148 to 2.205 Å (Table S5). The bond parameters computed by the full CASPT2 geometry optimization also agree very well with those obtained by point-wise CASPT2 calculations with values ranging from 1.918 to 1.941 Å for the LS and 2.146 to 2.149 Å for the HS states.[12]

3.3.3 Geometries of the Asymmetric $[Fe(pic)_3]^{2+}$ Complex

The geometries of the octahedral Fe(II) complexes discussed previously have relatively symmetric ligands and the CASPT2 geometries are in good agreement with literature data. However, one motivation for performing a full CASPT2 geometry optimization is when mixed ligand systems are employed, reducing the symmetry of the molecule. A point-wise optimization of each Fe–L bond distance becomes more challenging since one can no longer isotropically distort the octahedral field. Furthermore, the complex could involve a mixture of ligand field strengths. In this section we will examine the performance of CASPT2 geometry optimizations for an octahedral Fe(II) complex with asymmetric ligands, $[Fe(pic)_3]^{2+}$, where pic = 2-picolylamine (Figure 2).

In $[Fe(pic)_3]^{2+}$, the Fe center is in an octahedral field; however, two types of nitrogen atoms are present: the nitrogen in heterocyclic pyridine ring and the one in the aliphatic amine group. Kusz *et al.* reported the HS and LS geometries of the complex at different temperatures starting from 10K to 200K. At 10K, the average LS $Fe-N_{pyridine}$ bond distance was reported to be 1.995 Å, while the average $Fe-N_{amine}$ bond distance was 2.022 Å.[55] The Fe–N distances in the 100K LS geometry were similar to those reported at 10K with values of 2.006 Å for $Fe-N_{pyridine}$ and 2.029 Å for $Fe-N_{amine}$ (0.011 and 0.007 Å longer with respect to the 10 K structure).[55] They further demonstrated that the complex undergoes light-induced spin-crossover at 10K temperature and were able to characterize the structure of the complex in the HS state at 10 K.[55] The HS geometry has average bond distances of 2.208 Å for $Fe-N_{pyridine}$ and 2.182 Å for $Fe-N_{amine}$. Similar to the LS state, the average Fe–N distances in the structure of the HS state characterized at 200 K were similar to those at 10 K with values of 2.201 Å for $Fe-N_{pyridine}$ and 2.180 Å for $Fe-N_{amine}$ (0.007 and 0.002 Å shorter with respect to the 10K structure). Furthermore, Hostettler *et al.* showed that the structure is not particularly sensitive to choice of solvent.[56] Given these experimental results, we feel more comfortable comparing calculated gas phase Fe–N distances and experiment directly than we did for the previous complexes; however, the effect of crystal packing can be important and for this reason we continue to compare of DFT and CASPT2 directly as well.

For the LS geometry, the CASPT2 computed $Fe-N_{pyridine}$ bond distance was 1.964 Å, which is 0.031 Å shorter than the experimental value at 10K and 0.042 Å shorter than the value at 100K. The LS CASPT2 $Fe-N_{amine}$ distance was 2.029 Å in excellent agreement with those reported experimentally, which is 0.007 Å longer than the 10K structure and equal to the distance measured at 100 K. The average CASPT2 HS $Fe-N_{pyridine}$ bond distance is 2.187 Å which is 0.021 Å from the 10K geometry and 0.014 Å from the 200K geometry. The computed HS $Fe-N_{amine}$ bond distance is 2.234 Å on average, which is 0.052 and 0.054 Å longer than those characterized at 10K and 200K, respectively. Although gas phase optimizations do not account for crystal packing or thermal effects, the CASPT2 optimization could reproduce the small differences in the Fe–$N_{pyridine}$ and Fe–N_{amine} distances. Furthermore, the differences beteen CASPT2 and experiment were similar in magnitude to the deviations we obtained between DFT and CASPT2 in previous sections.

If we compare with DFT directly, a similar pattern emerges (Table S6). Taking the DFT geometries (PBE, M06-L, M06, and TPSSH), the Fe–$N_{pyridine}$ distances deviate from CASPT2 distances by 0.006 to 0.049 Å for the LS state and by -0.006 to 0.015 Å for the HS state. However, the Fe–N_{amine} distances vary by 0.022 to 0.043 Å for the LS state and 0.028 to 0.045 Å for the HS state. Once more, nice agreement between CASPT2 and DFT is observed with slightly better agreement between the methods for the Fe–$N_{pyridine}$ distances compared to the Fe–N_{amine} distances.

3.4 Computational Time

Finally, we report timings for a subset of the calculations performed (Table 5). All timings were computed on Intel SkyLake 5000 series dual 12-core nodes. The data in Table 5 are intended to be representative of the wall time and resources required for the computations in this work. The force calculations were performed on the FIC-CASPT2 optimized geometry, starting from the converged CASSCF calculation using the (10*e*, 12*o*) active space. However, we emphasize that the total time to optimize

the molecules depends on the quality of the guess geometry and the geometry optimization algorithm itself.

CASPT2 nuclear gradient theory has been recently reviewed,[36] but it is worth noting that the Lagrangian approach is used in which the so-called λ-equation is solved to determine the values of the Lagrange multipliers. It is this equation and the computation of the CASPT2 energy that require the most computational time. Therefore, the time is also reported for both of these, despite being included in the total gradient wall time.

The timings presented here are intended to show that the current version of the code can be used for applications with transition metals. The parallelization of the code and the implementation of advanced quasi-newton optimization methods such as the eigenvector following (EF) and the rational functional optimization (RFO) algorithms have made this work feasible.[82,83] In these computations, the EF algorithm was employed and the only convergence issues encountered were a resolved by increasing the size of the active space or by including a triple-ζ basis set on iron. As is the case with DFT geometry optimizations, larger molecules will require more geometry steps to converge.

Table 5 Computational time in seconds for the CASPT2 energy, λ-equation, and gradient evaluation using the ($10e$, $12o$) active space. The cc-pVTZ basis set was used on Fe and the cc-pVDZ basis set was employed for the remaining atoms.

	CPUs		Time (sec)		
Complex	Used	Spin	CASPT2 E	λ Eqn.	Gradient
$[Fe(PH_3)_6]^{2+}$	96	HS	556	476	1872
(25 Atoms)	192	HS	376	318	1364
(266 Basis)	288	HS	308	261	1191
	96	LS	186	214	826
	192	LS	127	146	584
	288	LS	105	118	509
$[Fe(pic)_3]^{2+}$	192	HS	3036	1838	7505
(49 Atoms)	288	HS	2413	1432	6066
(524 Basis)	384	HS	2039	1214	5095
	192	LS	938	1192	3257
	288	LS	732	936	2636
	384	LS	632	815	2265
$[Fe(bpy)_3]^{2+}$	288	HS	3575	2569	12060
(61 Atoms)	384	HS	2866	1950	9309
(692 Basis)	576	HS	2303	1462	7388
	288	LS	1334	1796	5649
	384	LS	1097	1395	4511
	576	LS	898	1124	3786

4 Conclusions

We have investigated the performance of FIC-CASPT2 analytical gradients to perform geometry optimization of a series of Fe(II) SCO complexes. An active space of ($10e$,$12o$), together with the cc-pVTZ basis set, was employed to optimize small $[FeL_6]^{2+}$ complexes, where the ligands L were chosen with varying ligand field strength. Comparisons between the CASPT2 geometries and crystal structures are less direct; therefore, we compared the CASPT2 geometries with those obtained by various DFT functionals and observe good agreement. Next, we optimize the geometries of comparatively larger complexes by means of CASPT2. Since the computational cost increases with system size, we employed different combinations of active spaces and basis sets to demonstrate the sensitivity of the geometry to these choices. Although the geometries are not particularly sensitive to active space choice, the convergence to a minima was improved by using the ($10e$,$12o$) active space. The iron center should be treated with cc-pVTZ basis set, but the cc-pVDZ basis set can be used on the remainder of the atoms without seriously impacting the quality of the geometry. CASPT2 computed geometries for the larger complexes ($[Fe(tacn)_2]^{2+}$, $[Fe(bpy)_3]^{2+}$, and $[Fe(pic)_3]^{2+}$) are in good agreement with DFT and those reported experimentally. This study focused on Fe(II) complexes that are expected to have reasonable geometries with DFT but provides support that moderate sized basis sets and active spaces can be used for other complexes, both in the ground and excited state, where multiconfigurational effects are more pronounced. In addition to our recent work on Cr2 complexes,[47] systems known for multiconfigurational electronic structures including other metal–metal bonds, complexes with non-innocent ligands, transition sates, intermediate spin states, and minima on excited state surfaces are expected to exhibit larger differences in molecular geometry between DFT and CASPT2 than those in this work.

Acknowledgements

This work was supported by the Department of Energy, Office of Science, Basic Energy Sciences grant No. DE-SC0019463. Computations supporting this project were performed on High Performance Computing systems at the University of South Dakota, funded by NSF Award OAC-1626516, and at the National Energy Research Scientific Computing Center (NERSC), a U.S. Department of Energy Office of Science User Facility operated under Contract No. DE-AC02-05CH11231.

Notes and references

1 A. Bousseksou, G. Molnár and G. Matouzenko, *Eur. J. Inorg. Chem.*, 2004, **2004**, 4353–4369.
2 M. A. Halcrow, *Spin-Crossover Materials: Properties and Applications*, John Wiley & Sons, Ltd., 2013.
3 D. C. Ashley and E. Jakubikova, *Coord. Chem. Rev.*, 2017, **337**, 97–111.
4 L. Cambi and L. Szegö, *Ber. dtsch. Chem. Ges. A/B,*, 1931, **64**, 2591–2598.
5 L. Cambi and L. Szegö, *Ber. dtsch. Chem. Ges. A/B,*, 1933, **66**, 656–661.
6 E. Koenig and K. Madeja, *Inorg. Chem.*, 1967, **6**, 48–55.
7 P. Gamez, J. S. Costa, M. Quesada and G. Aromí, *Dalton Trans.*, 2009, 7845–7853.
8 G. Molnár, L. Salmon, W. Nicolazzi, F. Terki and A. Bousseksou, *J. Mater. Chem. C*, 2014, **2**, 1360–1366.
9 A. Hauser, in *Ligand Field Theoretical Considerations*, ed. P. Gütlich and H. A. Goodwin, Springer Berlin Heidelberg, Berlin, Heidelberg, 2004, pp. 49–58.
10 M. Swart and M. Gruden, *Acc. Chem. Res.*, 2016, **49**, 2690–

2697.
11 C. de Graaf and C. Sousa, *Chem. Eur. J.*, 2010, **16**, 4550–4556.
12 K. Pierloot and S. Vancoillie, *J. Chem. Phys.*, 2006, **125**, 124303.
13 K. Pierloot and S. Vancoillie, *J. Chem. Phys.*, 2008, **128**, 034104.
14 H. Paulsen, L. Duelund, H. Winkler, H. Toftlund and A. X. Trautwein, *Inorg. Chem.*, 2001, **40**, 2201–2203.
15 M. Swart, *J. Chem. Theory Comput.*, 2008, **4**, 2057–2066.
16 S. R. Chowdhury and S. Mishra, *J. Chem. Phys*, 2018, **149**, 234302.
17 C. J. Cramer and D. Truhlar, *Phys. Chem. Chem. Phys.*, 2009, **11**, 10757–10816.
18 M. Reiher, *Inorg. Chem.*, 2002, **41**, 6928–6935.
19 M. Reiher, O. Salomon and B. A. Hess, *Theor. Chem. Acc.*, 2001, **107**, 48–55.
20 M. Pápai, G. Vankó, C. de Graaf and T. Rozgonyi, *J. Chem. Theory Comput.*, 2013, **9**, 509–519.
21 Q. M. Phung, M. Feldt, J. N. Harvey and K. Pierloot, *J. Chem. Theory Comput.*, 2018, **14**, 2446–2455.
22 C. Riplinger and F. Neese, *J. Chem. Phys.*, 2013, **138**, 034106.
23 C. Riplinger, B. Sandhoefer, A. Hansen and F. Neese, *J. Chem. Phys.*, 2013, **139**, 134101.
24 D. G. Liakos, M. Sparta, M. K. Kesharwani, J. M. L. Martin and F. Neese, *J. Chem. Theory. Comput.*, 2015, **11**, 1525–1539.
25 D. G. Liakos and F. Neese, *J. Chem. Theory. Comput.*, 2015, **11**, 4054–4063.
26 B. O. Roos, P. R. Taylor and P. E. Sigbahn, *Chem. Phys.*, 1980, **48**, 157–173.
27 B. O. Roos, *Int. J. Quantum Chem.*, 1980, **18**, 175–189.
28 K. Andersson, P. Malmqvist, B. O. Roos, A. J. Sadlej and K. Wolinski, *J. Phys. Chem.*, 1990, **94**, 5483–5488.
29 K. Andersson, P. Malmqvist and B. O. Roos, *J. Chem. Phys.*, 1992, **96**, 1218–1226.
30 P. Pulay, *Int. J. Quantum Chem.*, 2011, **111**, 3273–3279.
31 S. Vancoillie, H. Zhao, M. Radoń and K. Pierloot, *J. Chem. Theory Comput.*, 2010, **6**, 576–582.
32 K. Pierloot, Q. Phung and A. Domingo, *J. Chem. Theory Comput.*, 2017, **13**, 537–553.
33 M. K. MacLeod and T. Shiozaki, *J. Chem. Phys.*, 2015, **142**, 051103.
34 B. Ordejón, C. de Graaf and C. Sousa, *J. Am. Chem. Soc.*, 2008, **130**, 13961–13968.
35 J. Starling, A. Bernhardsson and R. Lindh, *Mol. Phys.*, 2001, **99**, 103–114.
36 J. W. Park, R. Al-Saadon, M. K. MacLeod, T. Shiozaki and B. Vlaisavljevich, *Chem. Rev.*, 2020, **120**, 5878–5909.
37 T. Shiozaki, *WIREs Comput. Mol. Sci.*, 2018, **8**, e1331.
38 B. Vlaisavljevich and T. Shiozaki, *J. Chem. Theory Comput.*, 2016, **12**, 3781–3787.
39 D. Theis, Y. G. Khait and M. R. Hoffmann, *J. Chem. Phys.*, 2011, **135**, 044117.
40 T. J. Dudley, Y. G. Khait and M. R. Hoffmann, *J. Chem. Phys.*, 2003, **119**, 651–660.
41 H. Nakano, K. Hirao and M. S. Gordon, *J. Chem. Phys.*, 1998, **108**, 5660–5669.
42 R. Shepard, H. Lischka, P. G. Szalay, T. Kovar and M. Ernzerhof, *J. Chem. Phys.*, 1992, **96**, 2085–2098.
43 T. Shiozaki, W. Gyorffy, P. Celani and H. J. Werner, *J. Chem. Phys.*, 2011, **135**, 081106.
44 P. Celani and H. J. Werner, *J. Chem. Phys.*, 2003, **119**, 5044–5057.
45 W. Gyorffy, T. Shiozaki, G. Knizia and H. J. Werner, *J. Chem. Phys.*, 2013, **138**, 104104.
46 J. W. Park, R. Al-Saadon, N. E. Strand and T. Shiozaki, *J. Chem. Theory Comput.*, 2019, **15**, 4088–4098.
47 T. Shiozaki and B. Vlaisavljevich, Inorg. Chem. 2021, ASAP, DOI: 10.1021/acs.inorgchem.1c03005.
48 B. M. Flöser, Y. Guo, C. Riplinger, F. Tuczek and F. Neese, *J. Chem. Theory Comput.*, 2020, **16**, 2224–2235.
49 L. A. Mariano, B. Vlaisavljevich and R. Poloni, *J. Chem. Theory Comput.*, 2020, **16**, 6755–6762.
50 L. A. Mariano, B. Vlaisavljevich and R. Poloni, *J. Chem. Theory Comput.*, 2021, **17**, 2807–2816.
51 L. Wilbraham, P. Verma, D. G. Truhlar, L. Gagliardi and I. Ciofini, *J. Phys. Chem. Lett.*, 2017, **8**, 2026–2030.
52 K. P. Kepp, *Inorg. Chem.*, 2016, **55**, 2717–2727.
53 R. L. Lord, F. A. Schultz and M. Baik, *J. Am. Chem. Soc.*, 2009, **131**, 6189–6197.
54 J. C. A. Boeyens, A. Forbes, R. D. Hancock and K. Wieghardt, *Inorg. Chem.*, 1985, **24**, 2926–2931.
55 J. Kusz, D. Schollmeyer, H. Spiering and P. Gütlich, *J. Appl. Cryst.*, 2005, **38**, 528–536.
56 M. Hostettler, K. W. Törnroos, D. Chernyshov, B. Vangdal and H. Bürgi, *Angew. Chem. Int. Ed.*, 2004, **43**, 4589–4594.
57 S. Dick, *Z. Kristallogr. New Cryst. Struct.*, 1998, **213**, 356.
58 A. Addala, Z. Setifi, Y. Morimoto, B. Artetxe, T. Matsumoto, J. M. Gutiérrez-Zorrill and C. Glidewell, *Acta Cryst. E*, 2018, **74**, 1717–1726.
59 L. M. L. Daku, A. Vargas, A. Hauser, A. Fouqueau and M. E. Casida, *ChemPhysChem*, 2005, **6**, 1393–1410.
60 *BAGEL, Brilliantly Advanced General Electronic-structure Library.*, `http://www.nubakery.org`, under the GNU General Public License.
61 N. B. Balabanov and K. A. Peterson, *J. Chem. Phys.*, 2005, **123**, 064107.
62 T. H. Dunning, *J. Chem. Phys.*, 1989, **90**, 1007–1023.
63 F. Weigend, *Phys. Chem. Chem. Phys.*, 2006, **8**, 1057–1065.
64 K. Andersson and B. O. Roos, *Chem. Phys. Lett.*, 1992, **191**, 507–514.
65 B. O. Roos and P. Malmqvist, *Phys. Chem. Chem. Phys.*, 2004, **6**, 2919–2927.
66 J. Paier, R. Hirschl, M. Marsman and G. Kresse, *J. Chem. Phys.*, 2005, **122**, 234102.
67 J. Tao, J. P. Perdew, V. N. Staroverov and G. E. Scuseria, *Phys. Rev. Lett.*, 2003, **91**, 146401.

68 V. N. Staroverov, G. E. Scuseria, J. Tao and J. P. Perdew, *J. Chem. Phys.*, 2004, **121**, 11507–11507.

69 Y. Zhao and D. G. Truhlar, *Theor. Chem. Acc.*, 2008, **120**, 215–241.

70 Y. Zhao and D. G. Truhlar, *J. Chem. Phys.*, 2006, **125**, 194101.

71 F. Weigend and R. Ahlrichs, *Phys. Chem. Chem. Phys.*, 2005, **7**, 3297.

72 S. G. Balasubramani, G. P. Chen, S. Coriani, M. Diedenhofen and e. a. M. Frank, *J. Chem. Phys.*, 2020, **152**, 184107.

73 K. Eichkorn, O. Treutler, H. Öhm, M. Häser and R. Ahlrichs, *Chem. Phys. Lett.*, 1995, **242**, 652–660.

74 F. Neese, *WIREs Comput. Mol. Sci.*, 2012, **2**, 73–78.

75 F. Neese, *WIREs Comput. Mol. Sci.*, 2018, **8**, e1327.

76 E. Bernhardt, B. Bley, R. Wartchow, H. Willner, E. Bill, P. Kuhn, I. H. T. Shama, M. Bodenbinder, R. Bröchler and F. Aubke, *J. Am. Chem. Soc.*, 1999, **121**, 7188–7200.

77 G. Constant, J. C. Daran and Y. Jeannin, *J. Inorg. Nucl. Chem.*, 1973, **35**, 4093–4102.

78 A. S. Tolla, A. Banerjee, S. Stjepanovic, J. Li, W. W. Brennessel, R. Loloee and F. A. Chavez, *Eur. J. Inorg. Chem.*, 2013, **2013**, 2115–2121.

79 A. Rudavskyi, C. Sousa, C. de Graaf, R. W. A. Havenith and R. Broer, *J. Chem. Phys.*, 2014, **140**, 184318.

80 A. Cannizzo, C. Milne, C. Consani, W. Gawelda, C. Bressler, F. van Mourik and M. Chergui, *Coord. Chem. Rev.*, 2010, **254**, 2677–2686.

81 G. Auböck and M. Chergui, *Nat. Chem.*, 2015, **7**, 629–633.

82 J. Baker, *J. Comput. Chem.*, 1986, **7**, 385–395.

83 A. Banerjee, N. Adams, J. Simons and R. Shepar, *J. Phys. Chem.*, 1985, **89**, 52–57.